How to cite: Angew. Chem. Int. Ed. 2024, e202402840
doi.org/10.1002/anie.202402840

VIP Solar Cells Very Important Paper

Cascade Reaction in Organic Hole Transport Layer Enables Efficient Perovskite Solar Cells

Zhineng Lan[+], Hao Huang[+], Shuxian Du, Yi Lu, Changxu Sun, Yingying Yang, Qiang Zhang, Yi Suo, Shujie Qu, Min Wang, Xinxin Wang, Luyao Yan, Peng Cui, Zhiguo Zhao, and Meicheng Li**

Abstract: The doped organic hole transport layer (HTL) is crucial for achieving high-efficiency perovskite solar cells (PSCs). However, the traditional doping strategy undergoes a time-consuming and environment-dependent oxidation process, which hinders the technology upgrades and commercialization of PSCs. Here, we reported a new strategy by introducing a cascade reaction in traditional doped Spiro-OMeTAD, which can simultaneously achieve rapid oxidation and overcome the erosion of perovskite by 4-tert-butylpyridine (tBP) in organic HTL. The ideal dopant iodobenzene diacetate was utilized as the initiator that can react with Spiro to generate $Spiro^{\bullet+}$ radicals quickly and efficiently without the participation of ambient air, with the byproduct of iodobenzene (DB). Then, the DB can coordinate with tBP through a halogen bond to form a tBP-DB complex, minimizing the sustained erosion from tBP to perovskite. Based on the above cascade reaction, the resulting Spiro-based PSCs have a champion PCE of 25.76 % (certificated of 25.38 %). This new oxidation process of HTL is less environment-dependent and produces PSCs with higher reproducibility. Moreover, the PTAA-based PSCs obtain a PCE of 23.76 %, demonstrating the excellent applicability of this doping strategy on organic HTL.

Introduction

Metal halide perovskite solar cells (PSCs) have achieved considerable advances in power conversion efficiency (PCE) in the last decade, with the certificated PCE up to 26 % at present.[1–4] Such PCE progress mainly comes from rapid technology upgrades, as the fabrication cycle of PSCs is <24 hours.[5–7] Currently, the high-efficiency PSCs (PCE >24 %) with an n-i-p structure utilize organic materials as the hole transport layer (HTL), the represented materials is Spiro-OMeTAD (we name it Spiro in the latter discussion).[8,9] However, the pristine Spiro needs an oxidation process, commonly exposure to ambient air, to obtain high conductivity and suitable energy level matching with perovskite, supporting the realization of high-efficiency PSCs.[10,11] This oxidation process usually lasts for dozens of hours, and the oxidation effect depends on ambient conditions. The time-intensive and difficult-controlled oxidation process largely postpones the performance feedback and impacts the repeatability, thus hindering the technology upgrades and efficiency improvement.

The conventional recipe of Spiro HTL is composed of Spiro, lithium bis(trifluoromethane)sulfonimide (LiTFSI) and 4-tert-butylpyridine (tBP).[2] The LiTFSI is used to facilitate the generation of $Spiro^{\bullet+}$ radicals, and the tBP is used to accelerate the dissolution of LiTFSI and optimize the film morphology.[12,13] To overcome the challenge of long-time oxidation, which is necessary for this recipe, researchers have made a lot of effort. As early as 2014, William H. Nguyen and the co-worker directly incorporated the radical of $Spiro(TFSI)_2$ into the Spiro precursor to enhance the hole-conductivity without oxidation, which was followed up and further modified by Gao's group in 2022, who proposed a strategy of ion-modulated radical doping to achieve PCE of >25 % in time at Spiro based PSCs.[11,14] Oxidants, such as benzoyl peroxide, chromium trioxide, I_2, and so on, have been used to shorten the oxidation time for obtaining high-efficiency PSCs.[15–18] Recently, Li's group synthesized a series of iodonium salts with strong oxidizing properties to manipulate the oxidation states of Spiro without air assistance, leading to the PSCs possessing an excellent PCE of 25.16 %.[19] Except for the issue of time-consuming oxidation, the tBP, which is used to accelerate the dissolution of LiTFSI and optimize the film morphology, should also be carefully addressed. Francesco Lamberti and his co-workers reported that the tBP can de-dope Spiro, negatively impacting on its electrical properties.[20] Moreover, the detrimental impact of tBP on perovskite film has also been proved. Wang's group, Bi's group, and Guo's group reported that the tBP could erosion perovskite film by forming tBP-PbI_2 complex, which induces the decom-

[*] Z. Lan,[+] H. Huang,[+] S. Du, Y. Lu, C. Sun, Y. Yang, Q. Zhang, Y. Suo, S. Qu, M. Wang, X. Wang, L. Yan, P. Cui, Prof. Dr. M. Li
North China Electric Power University
State Key Laboratory of Alternate Electrical Power System with Renewable Energy Sources
2 Beinong Road, Changping District, Beijing 102206, China
E-mail: mcli@ncepu.edu.cn
Prof. Dr. Z. Zhao
China Huaneng Clean Energy Research Institute, Beijing 102209, China
E-mail: zhao_zg@qny.chng.com.cn
[+] These authors contributed equally.

position at the perovskite/Spiro interface and further affects the stability of PSCs.[21–23] Furtherly, 1,6-diazidohexane and 1,4-diiodotetra-fluorobenzene were adopted into the Spiro precursor to lock the tBP, which can minimize the formation of tBP-PbI_2 complex. Based on the above analysis, it is necessary to carefully address both the issues of time-consuming oxidation and the sustained erosion of tBP on perovskite to maximize the advantage of Spiro, achieving ultrahigh-efficiency and stable PSCs with high reproducibility.

In this study, we proposed a cascade reaction strategy to achieve quick oxidation and overcome the perovskite erosion from tBP by incorporating an ideal dopant of iodobenzene diacetate (ID, shown in Figure S1). The ID possesses suitable oxidation capacity, which can capture electrons from Spiro molecule through an oxidation-reduction reaction.[24] This instant reaction can generate $Spiro^{\bullet+}$ radicals and iodobenzene (DB, shown in Figure S2) without the participation of ambient air. The generated DB, a molecule possessing a halogen bond donor, can serve as a locker of tBP by forming a tBP-DB complex through the chemical binding of halogen bond, which can effectively minimize the sustained erosion of perovskite. The doped Spiro based on our doping strategy makes the PSCs exhibit PCE up to 24.32 % immediately, a high efficiency enough to give a proper feedback of experiment during the technology upgrade, and a champion PCE of 25.76 % (certificated of 25.38 %) with good reproducibility and stability. In addition, this doping strategy also shows excellent applicability in other organic HTL. The PTAA-based PSCs obtain a high PCE of 23.76 %, and the P3HT-based PSCs obtain a PCE of 21.09 %.

Results and Discussion

Photovoltaic Performance Based on Spiro-ID

The conventional recipe of Spiro, including large amount of dopants (~56 mol % LiTFSI and ~330 mol % tBP), requires a time-consuming oxidation process with the participation of O_2 and H_2O in ambient air to improve property according to the following equation:[25]

$$2H_2O + O_2 + 4Spiro + LiTFSI \xrightarrow{yields} 4Spiro^{+}TFSI^{-} + 4LiOH \quad (1)$$

The participant of H_2O is prone to induce negative impact because the Spiro, including lithium salts, is sensitive to moisture, resulting in structure disruption of agglomeration.[26] Besides, the massive additive of tBP can form a tBP-PbI_2 complex, which causes a decomposition at the interface of perovskite/Spiro.[23] To address both the issue of the required long-term oxidation and erosion destruction on perovskite from tBP, we rationally incorporate ID into the Spiro (we name it the Spiro-ID) to produce dual functions through a cascade reaction. The first function is quick oxidation, and the second function is inhibition of the detrimental impact of tBP on perovskite (Figure 1a).

After incorporating the ID, we carried out the conductivity measurements on a batch of Spiro and Spiro-ID films. As shown in Figure 1b, the conductivity of Spiro-ID is nearly 4.5 times larger than that of Spiro, exhibiting excellent oxidation effects. When both the Spiro-ID and Spiro are exposed to ambient air, the conductivity of Spiro gradually increases with the increase of oxidation time in ambient air. In contrast, the conductivity of Spiro-ID shows minor changes, especially after 20 min. After 12 hours of oxidation, the average conductivity of 6 Spiro-based samples increases from 2.42×10^{-6} to 5.02×10^{-6} $S\,cm^{-1}$. However, this conductivity is still much smaller than that of 1.04×10^{-5} $S\,cm^{-1}$ of 6 Spiro-ID based samples and shows significant inconsistencies across samples. The standard deviation (SD) is used to assess reproducibility of samples, and the result showed an SD of 1.2×10^{-6} for Spiro-based samples and 1.1×10^{-7} for Spiro-ID-based samples, which indicates that the repeatability of Spiro-ID-based samples is about ten times than that of Spiro-based samples. The increased conductivity and reproducibility mainly result from the improved and reliable oxidation efficiency after incorporating ID. Similarly, the changes in hole mobility of Spiro films before and after the introduction of ID are also shown in Figure S3. We further monitored the PCE evolution of 60 PSCs structured as FTO/c-TiO_2/perovskite/MeO-PEAI/Spiro (Spiro-ID)/Au, with the oxidation time increasing in ambient air (Figure 1c). Obviously, the PSCs with Spiro-ID show higher PCE than those with Spiro, which is consistent with the conductivity measurement results. In detail, the best-performing PSC with Spiro-ID exhibits a PCE of 24.32 % immediately without air oxidation, much higher than that of the best-performing PSC with Spiro, a high efficiency enough to give proper feedback of experiment during the technology upgrade (Figure S4). As the oxidation time increases in ambient air, the average PCE gap between the different PSCs becomes smaller due to the obvious PCE increment of PSCs with Spiro. However, the PCE of PSCs with Spiro-ID is still higher than that of PSCs with Spiro. Except for the PCE improvement, it is noted that the PSCs′ reproducibility has been effectively improved, which is meaningful to the accurate evaluation of the availability of a new approach during the technology upgrade. After adequate oxidation, the PCE range of 60 PSCs with Spiro is from 20.16 % to 24.92 % with an SD of 0.96. As a comparison, the PCEs of 60 PSCs with Spiro-ID are distributed in a small range from 23.51 % to 25.28 % with an SD of 0.40, indicating that the repeatability of PCE of PSCs is improved by about 2.5 times. This improved reproducibility is mainly due to the regulated oxidation that decreases the reliance of PSCs performance on variant ambient air conditions. Impressively, Figure 1d and Table S1 exhibit the champion PCEs of both PSCs, where the PSC with Spiro-ID achieves a PCE of 25.76 % (certificated of 25.38 %, shown in Figure S5) and the PSC with Spiro achieves a PCE of 24.92 %. Figures S6 and S7 show the corresponding forward *J–V* curves, external quantum efficiency spectra, and integrated J_{sc}. The improved PCE should result from the dual function mentioned in the above discussion of Figure 1a. We further fabricated PSCs with a

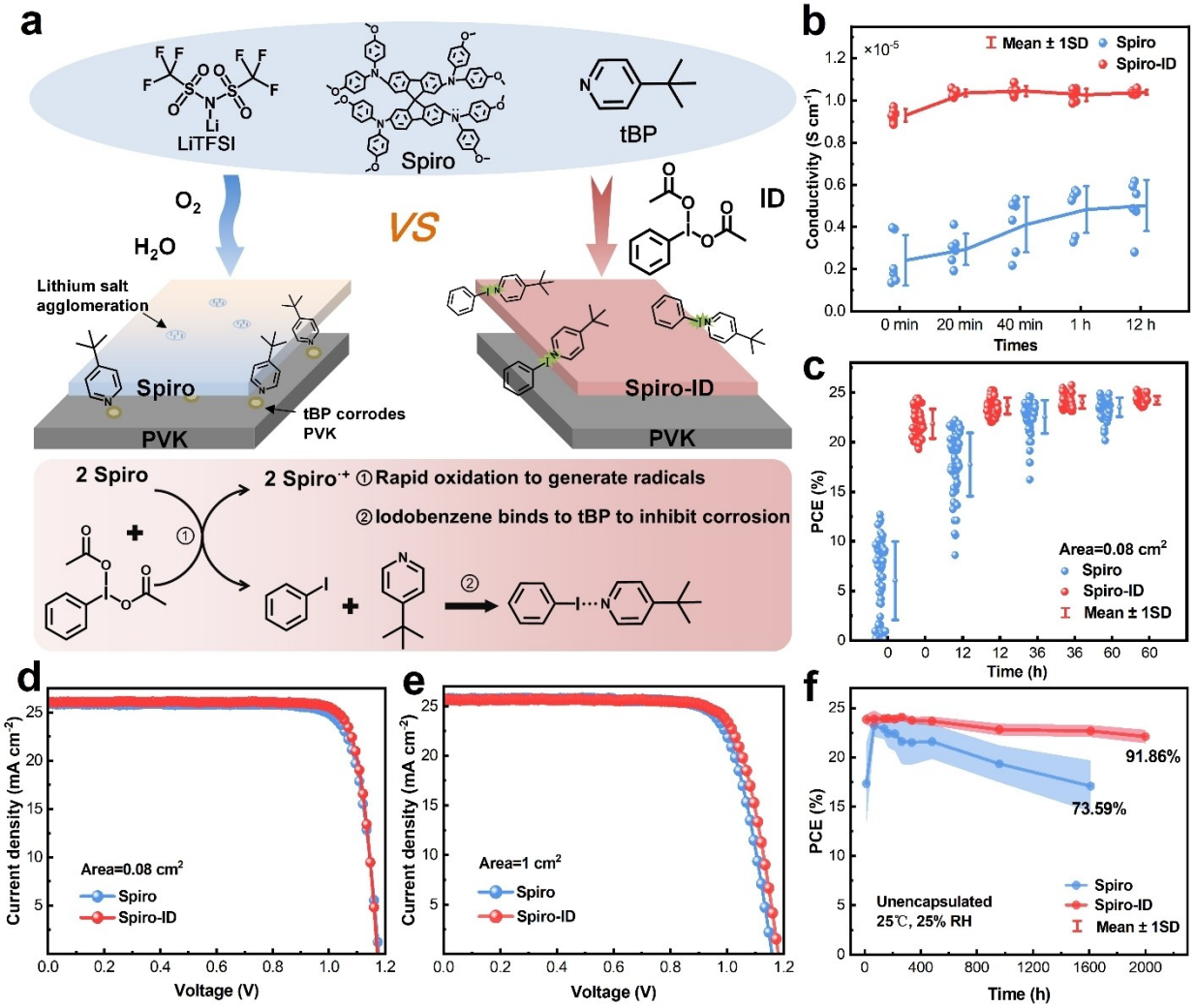

Figure 1. Photovoltaic performance of PSCs with different HTLs. (a) The schematic diagram of dual functions from cascade reaction of ID in Spiro. (b) The evolution of conductivity with oxidation time. (c) The evolution of PCE with oxidation time. (d) Reverse *J–V* curves of champion PSCs with different HTLs, the active area is 0.08 cm^2. (e) Reverse *J–V* curves of champion PSCs with different HTLs, the active area is 1 cm^2. (f) The PCE evolution of 10 unencapsulated PSCs with different HTLs aged in ambient air.

larger aperture area of 1 cm^2 to research the applicability of this new doped Spiro-ID in large-area PSCs. The PCE evolution of 20 PSCs with the oxidation time increasing in ambient air is shown in Figure S8. Moreover, the PSC with Spiro-ID possesses a champion PCE of 23.69 %, which is higher than that (23.03 %) of the PSC with Spiro, showing a good potential in efficient large-area PSCs (Figure 1e and Table S2).

Since the Spiro-ID can inhibit the erosion of tBP on perovskite, an improvement in device stability can be expected. We firstly monitored the PCE evolution of 10 samples in both devices, which are stored in ambient conditions with 25 % relative humidity (RH) and 25 °C. It is found that PSCs with Spiro show a noticeable PCE improvement in the first few dozen hours, which is due to the long-time oxidation process. We set the highest average PCE after adequate oxidation as the initial average PCE and evaluate the PCE decay based on this setting. After storage for 2000 hours, PSCs with Spiro-ID can maintain 91.86 % of their initial average PCE with a relatively uniform trend. Compared, the PSC with Spiro can only maintain 73.59 % of its initial PCE. The enhanced storage stability may have two reasons: the first one is the inhibition of perovskite sustained erosion at the interface of perovskite/Spiro-ID due to the formed complex of tBP-DB; the second one is ID-doped Spiro achieves rapid oxidation at the solution stage, which avoids the long-time hygroscopic oxidation in ambient air (Figure S9 and Note S1). We further investigated the device stability under conditions of high humidity and high temperature. respectively. After storage in humid conditions with 85 % relative humidity (RH) and 25 °C for 400 hours, PSCs with Spiro-ID can maintain 89.96 % of their initial average PCE, while the PSC with Spiro can only maintain 70.16 % of its initial PCE (Figure S10). The thermal stability of PSCs with Spiro-ID shows a similar enhancement (Figure S11). The results of operational stability are shown in Figure S12.

The PSCs with Spiro-ID can maintain ~90 % of the initial PCE after operating for 600 hours, while the PSCs with Spiro only maintained 75 % after operating for 400 hours.

Quick and Efficient Oxidation

The incorporated ID in Spiro can have dual functions from the cascade reaction, contributing to high-efficiency PSCs with high reproducibility. We have simply introduced these dual functions in the above discussion. Now, we are going to systematically conduct research and discuss quick and efficient oxidation, one of the dual functions. The later research is mostly carried out on Spiro film and Spiro-ID film. For an accurate characterization, these films are stored in an inert atmosphere or vacuum condition before measurements to rule out the interference of ambient air.

Figure 2a shows the cyclic voltammograms (C–V) curves of Spiro and ID, where the first oxidation potential of ID is 1.12 V, which is larger than that of Spiro (0.89 V). A potential difference of 0.23 V between the ID and Spiro can easily trigger the oxidation reaction.[27] The Fourier transform infrared spectroscopy was performed to explore the chemical states of ID after it is incorporated into Spiro. As shown in Figure 2b and Figure S13, the spectrum of ID shows a typical infrared signal at 1162 cm^{-1}, which is shared by the spectrum of Spiro-ID, indicating the successful incorporation of ID into the Spiro. Moreover, we can also notice an obvious infrared signal at 1572 cm^{-1} in Figure 2c, which is supposed to belong to the reaction product of DB (Figure S14). Various measurements, including UV/Visible (UV/Vis) spectroscopy, electron spin resonance (ESR), and photoluminescence (PL) spectra, were carried out to explore the Spiro$^{\bullet+}$ radicals, which can evaluate the oxidation effectiveness. As shown in Figure 2d, the solution of Spiro-ID exhibits obvious polaron absorption peaks centered at ~520 nm, which is reported to arise in oxidized Spiro.[28] We also monitored the change of the absorption peak strength of the film over time, in contrast to the Spiro-ID films, which quickly reached a maximum, while the Spiro films showed a sustained increase (Figure S15). This trend is consistent with changes in conductivity and PCE (Figures 1b and c). The changes in UV/Vis spectra are validated by the inset, where the color of the Spiro solution changes from light yellow to purplish red. The ESR spectrum of Spiro-ID film shows paramagnetic peaks at 3480–3520 G, further demonstrating the generated Spiro$^{\bullet+}$ radicals (Figure 2e).[29] In addition, except for utilizing the solution as the experiment sample, we also performed PL measurements on the Spiro and Spiro-ID films. As evidenced by the PL spectra in Figure 2f, the spectrum of Spiro-ID exhibits a significant peak quenching, indicating the existing Spiro$^{\bullet+}$ radicals.[9] Thus, we can propose that the ID possesses a strong oxidation capacity to trigger an oxidation reaction in the Spiro solution, leading to massive of Spiro$^{\bullet+}$ radicals generated quickly and efficiently.

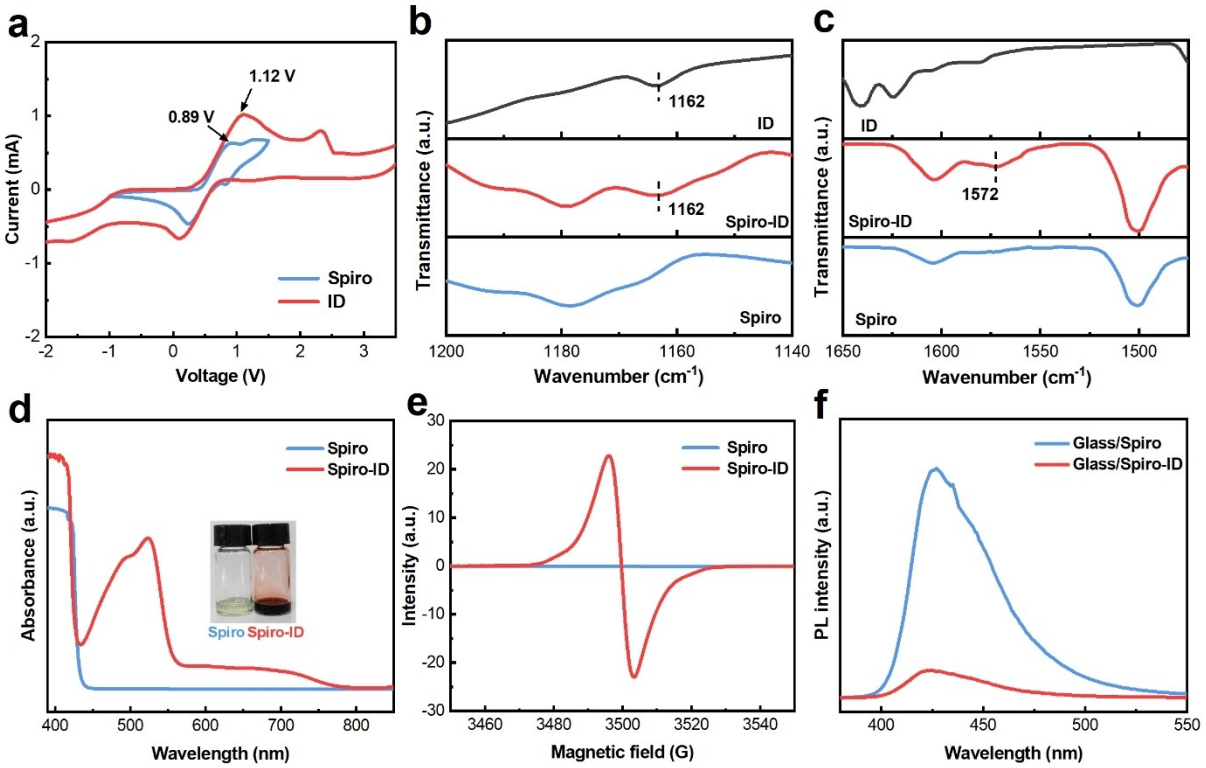

Figure 2. Characterization of quick and efficient oxidation. (a) C–V curves of Spiro and ID. (b, c) FTIR spectra of ID, Spiro and Spiro-ID. (d) Absorption spectra of Spiro and Spiro-ID, the samples are solutions. (e) ESR spectroscopy results of Spiro and Spiro-ID, the samples are films. (f) The PL spectra of Spiro and Spiro-ID, both the films are deposited on glass.

After ensuring the Spiro$^{\bullet+}$ radicals generated from oxidation reaction between Spiro and ID, we also evaluated the electrical properties of Spiro film and Spiro-ID. The conductive atomic force microscopy (c-AFM) images are shown in Figure S16, where the average current of Spiro film is 4.03 nA. The Spiro-ID film exhibits a high average current of 7.15 nA, which is consistent with the conductivity measurements in Figure 1b. Both the results of c-AFM and conductivity measurements prove that the ID can induce a quick and effective oxidation, leading to obvious improved conductivity of Spiro film. Considering the energy level structure, we firstly performed Kelvin probe force microscopy (KPFM) to evaluate the surface potential of different films. As shown in Figure 3a, the surface potential of Spiro-ID film is obviously higher than that of Spiro film, indicating that the Spiro-ID film possesses a lower Fermi level (E_F) and becomes more p-type than the Spiro film. Ultraviolet photoelectron spectroscopy (UPS) was utilized to characterize the detailed energy level structure. Figure 3b shows the UPS spectra of Spiro-ID film and Spiro film; after the incorporation of ID, the secondary electron cut-off ($E_{cut\text{-}off}$) edge of Spiro shifts from 17.26 eV to 16.81 eV, the corresponding E_F changes from −3.96 eV to −4.41 eV. Based on the obtained E_F, we can calculate the valence band maximum energy (E_{VBM}) value of Spiro film to be −4.97 eV and the E_{VBM} value of Spiro-ID film to be −5.09 eV. Combining the band gap value obtained from the Tauc plots (Figure S17), we can further calculate the conduction band minimum energy (E_{CBM}) value of Spiro film to be −2.00 eV and the E_{CBM} of Spiro-ID to be −2.13 eV. The results of UPS prove that the quick oxidation of ID can modulate the energy level structure of Spiro and make it to be more p-type, which is consistent with the results of KPFM. An optimal E_F of the HTL aligned with the quasi–Fermi level (QFL) of the perovskite layer is critical to minimize the voltage loss.[30,31] As illustrated in Figure 2d, the downshift of E_F resulting from the quick oxidation reduces the offset between the HTL and perovskite film. This change enables a high QFL spitting in the perovskite under illumination, which is beneficial for improving the open circuit voltage (V_{oc}) of final PSCs.

The improved conductivity and reduced energy level offset have been proved, which is supposed to enhance the interfacial carrier transport. The PL and time-resolved photoluminescence (TRPL) measurements were carried out to characterize the interfacial carrier transport dynamic. We

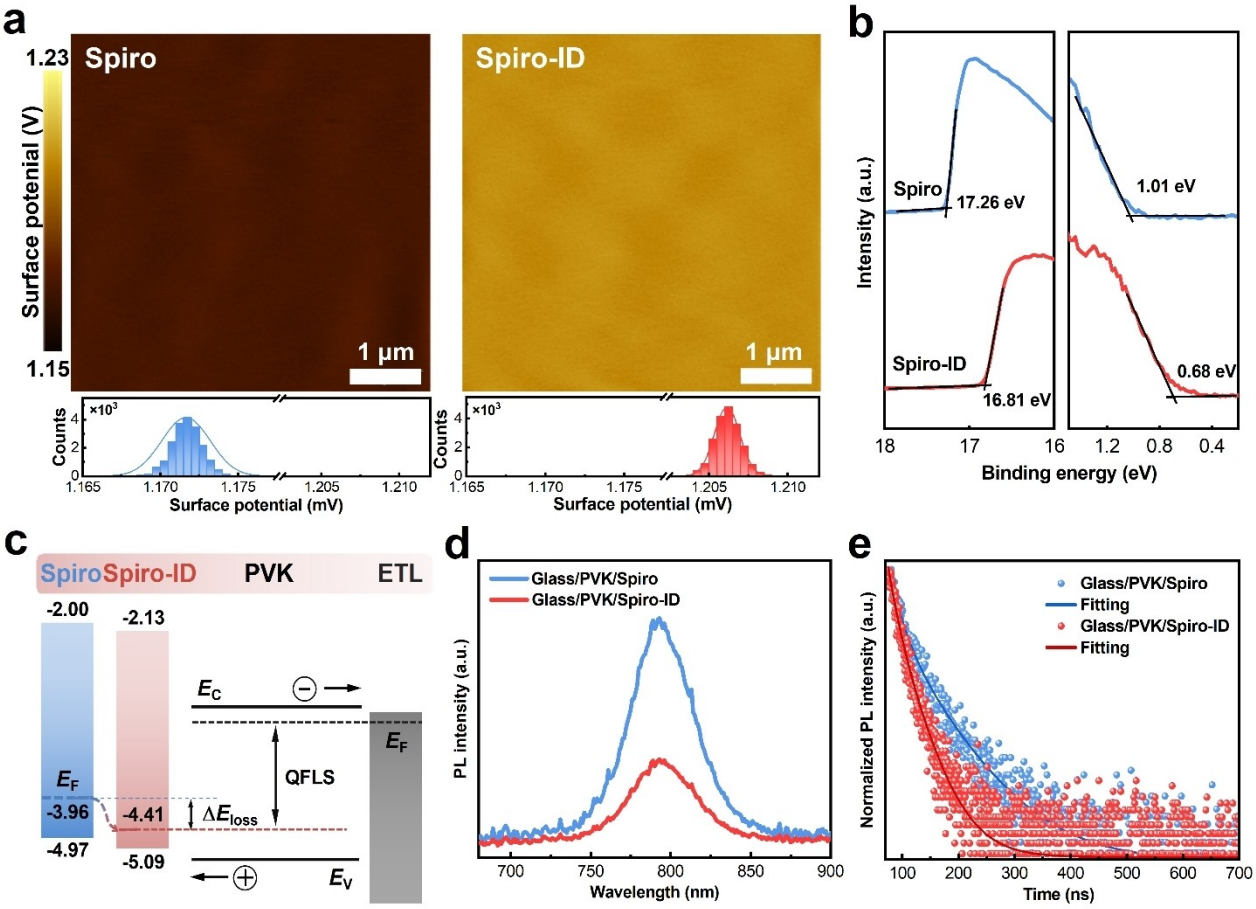

Figure 3. Electronic property of Spiro and Spiro-ID. (a) KPFM images and corresponding surface potential distribution of Spiro and Spiro-ID. (b) UPS spectra of Spiro and Spiro-ID. (c) Illustration of the band alignment between perovskite and HTLs. (d) PL spectra of glass/perovskite/Spiro (Spiro-ID) films. (e) TRPL spectra of glass/perovskite/Spiro (Spiro-ID) films.

fabricated samples structured as glass/perovskite/Spiro (Spiro-ID) and obtained PL and TRPL spectra when making the light incident from the glass side. Comparing the PL spectrum of perovskite under Spiro film, the PL spectrum of perovskite under Spiro film shows a significant quenching, indicating photogenerated carriers have been transmitted into Spiro-ID more efficiently (Figure 3d). The TRPL spectra and corresponding decay lifetime of the carrier are shown in Figure 3e. The decay lifetime (19 ns) of the perovskite under Spiro-ID is almost half of that (38 ns) of perovskite under Spiro, indicating that the carriers are extracted quickly at the interface of perovskite/Spiro-ID, which is consistent with the result of the PL measurement.

Overcoming Perovskite Erosion Induced by TBP

We are now turning to another function of incorporating the ID into Spiro, overcoming perovskite sustained erosion induced by tBP. In the discussion about quick oxidation, we mentioned that the ID can easily trigger an oxidation reaction with Spiro, generating Spiro$^{\bullet+}$ radicals. Actually, there is another reaction product, iodobenzene (DB), which is speculated through the chemical property of ID and proved by the FTIR measurements in Figure 2c. The DB possesses a halogen donor, which can form the tBP-DB complex through I···N bond (Figure 4a). We directly incorporated the DB into the tBP and then carried out FTIR measurement to explore their chemical interaction. As shown in Figure 4b, the spectrum of DB shows a series of absorption peaks in the range 1610–1370 cm^{-1} and 860–

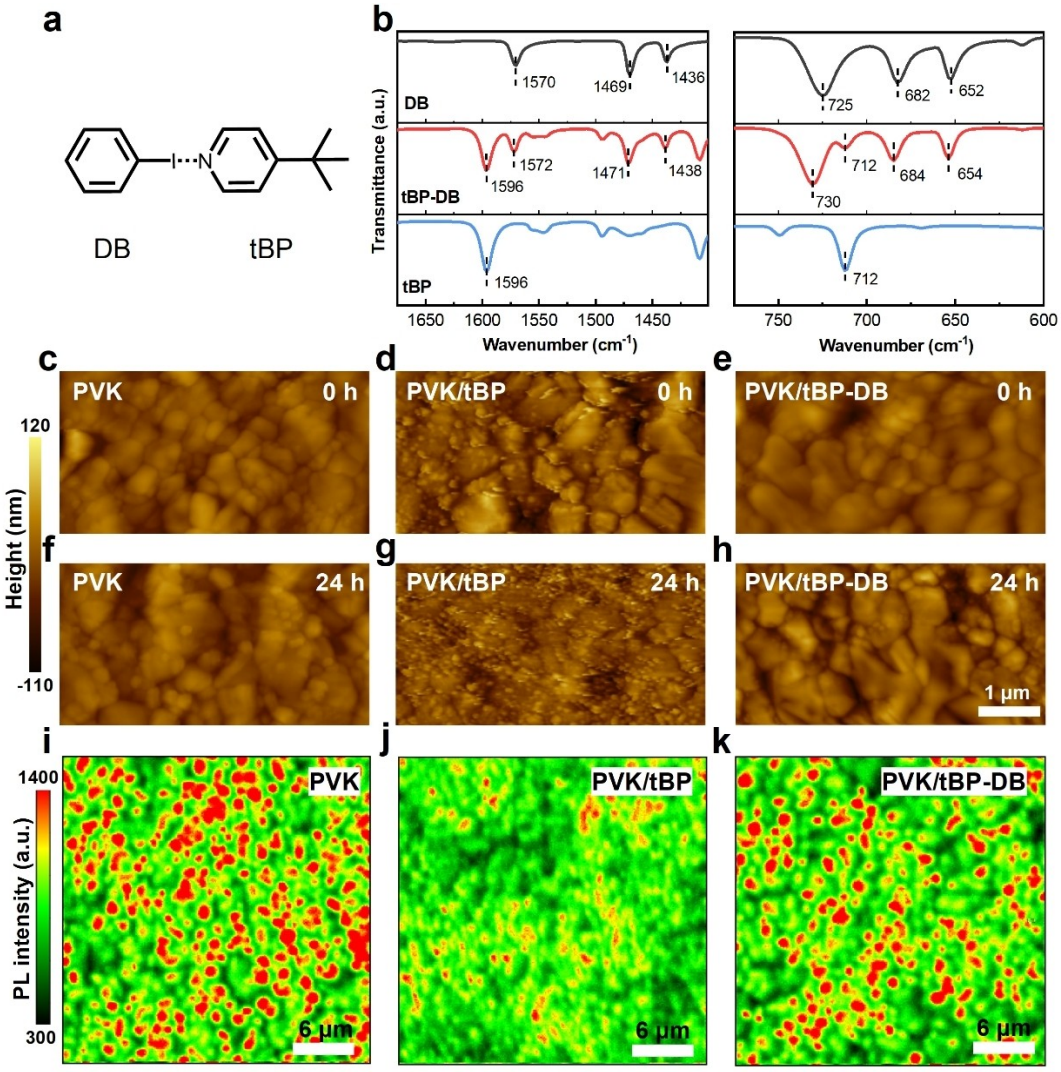

Figure 4. Overcoming the perovskite erosion induced by tBP. (a) Schematic diagram of tBP-DB complex. (b) FTIR spectra of DB, tBP-DB, and tBP. (c–e) AFM images of untreated perovskite film and perovskite films treated with tBP and tBP-DB steam for 5 minutes and then placed for 24 hours in N_2 glove box, respectively. (f–h) AFM images of untreated perovskite film and perovskite films treated with tBP and tBP-DB steam for 5 minutes and then placed for 24 hours in N_2 glove box, respectively. (i) PL mapping of perovskite film. (j) PL mapping of perovskite film after spin-coating tBP. (k) PL mapping of perovskite film after spin-coating tBP-DB.

$670\,cm^{-1}$, which are related to the stretching vibration of C=C and the bending vibration of =CH on the benzene ring, respectively. When DB and tBP are mixed, we can notice that these peaks shift significantly towards higher wavenumbers, which is consistent with the emergence of a new peak associated with DB in Spiro-ID with accompanying shifts (Figure 2c). These peaks shift is related to the formation of halogen bonds between tBP and DB and the transfer of electrons to other atoms around the halogen bonds.[22,23,32]

To demonstrate that the tBP-DB complex can effectively inhibit the perovskite erosion induced by tBP, we carried out an indirect experiment by spin-coating a tBP solution on perovskite films. The tBP solution with or without DB were prepared using chlorobenzene as the solvent, keeping the mole concentration the same as the Spiro solution. Firstly, the atomic force microscope (AFM) measurement was performed to characterize perovskite films. Figure S18 exhibits the AFM images of perovskite, perovskite/tBP, and perovskite/tBP-DB, respectively, and the corresponding photos are shown in the inset. After spin-coating tBP on the surface of perovskite, we can find that there is an obvious change from the AFM images, which is consistent with the color change of photos in the inset. In detail, the grain surface generates number of small fragments, which is mainly caused by tBP. The tBP can form a complex with PbI_2, which will destroy perovskite crystal structure and lead to a rough grain surface, just as shown in Figure S18b. After incorporating DB into the tBP solution, the tiny fragments located at the grain surface have been effectively decreased, and the perovskite film can maintain a similar color, which demonstrates the perovskite erosion induced by tBP has been inhibited by incorporating DB. We further treated perovskite films with tBP and tBP-DB steam for 5 minutes and put them in N_2 glovebox (Figure S19). We utilized AFM to monitor the surface changes of perovskite film to investigate the continuous erosion from tBP on perovskite. As shown in Figures 4c and 4f, after storage for 24 hours, the untreated perovskite film shows negligible change in surface morphology, indicating that the perovskite can be stable in N_2 glovebox. However, when perovskite film is treated by tBP steam, the perovskite surface shows decomposition with tiny fragments emerging at the grain boundary at once. The surface decomposition still keeps worsening after storage for 24 hours, indicating the tBP can continuously induce perovskite decomposition. As a comparison, the perovskite film treated by tBP-DB steam shows negligible changes in surface morphology and can remain relatively stable after storage for 24 hours. Even after storage for 288 hours, the perovskite film treated by tBP-DB steam only shows slight decomposition while the perovskite film treated by tBP steam shows a severe decomposition with a crushed surface structure (Figure S20). The reason for the minimized perovskite erosion is the formation of the tBP-DB complex, which weakens the chemical reactivity and decreases the formation of the tBP-PbI_2 complex. The formation of the tBP-PbI_2 complex will induce a large number of defects on the surface of perovskite and further cause perovskite decomposition, which is the primary way to lead to serious non-radiative carrier recombination and cause sustained damage and further decrease stability.[23] As shown in Figures 4i–4k, the average PL intensity 850 of perovskite/tBP is smaller than that 1010 of perovskite, indicating that there is increased non-radiative carrier recombination in the perovskite surface after spin-coating tBP. Expectedly, the average PL intensity has been increased after incorporating the DB into the tBP, compared to that of perovskite/tBP, which demonstrates the DB can decrease the surface non-radiative carrier recombination because it can minimize the perovskite erosion induced by tBP. Both the results of AFM and PL mapping prove that the DB, a reaction product of ID, can effectively protect perovskite from tBP disruption, which contributes to decreasing the non-radiative carrier recombination at perovskite/Spiro interface and further obtaining high-efficiency PSCs.

Available in π-Conjugated Polymers

The dual functions from the cascade reaction of ID in Spiro have been proved to effectively improve the photovoltaic performance and reproducibility of PSCs. This modification approach is expected to be available on other π-conjugated polymers that are reported as HTL in PSCs. We incorporated ID into two representative conjugated polymers: poly[bis(4-phenyl)(2,4,6-trimethylphenyl)amine] (PTAA) and poly(3-hexylthiophene-2,5-diyl) (P3HT). As evidenced by the PL spectra and photo in Figures 5a and 5d and the corresponding inset, the ID can induce quick oxidation of PTAA and P3HT and further enhance their hole extraction ability. The results of UV/Vis spectra, ESR, and conductivity also show the oxidation capacity of ID (Figures S21–25). As for the PSCs with PTAA, the PSCs with PTAA-ID (PTAA incorporated with ID) achieve a champion PCE of 23.76 %, with a short circuit current density (J_{sc}) of $25.74\,mA\,cm^{-2}$, a fill factor (FF) of 80.44 % and a V_{oc} of 1.148 V. As a comparison, the PSCs with PTAA only achieve a champion PCE of 21.79 %, with a J_{sc} of $25.51\,mA\,cm^{-2}$, an FF of 77.10 % and a V_{oc} of 1.108 V (Figure 5b and Table S3). We collected photovoltaic parameters of 25 PSCs with PTAA and PSCs with PTAA-ID, respectively. The increased average PCE and enhanced reproducibility have been demonstrated after incorporating ID into PTAA (Figure 5c and Figure S26). The similar positive effects of ID on PSCs performance have also been validated when using the P3HT as HTL. As shown in Figure 5e and Table S4, after incorporating ID into P3HT, the champion PCE of PSCs increases from 20.21 % to 21.09 %, and the average PCE of 25 PSCs increases from 17.44 % to 19.54 % (Figure 5f and Figure S27). These improvements in PSC's photovoltaic performance are expected when the electronic property of HTL has been enhanced and the detrimental erosion at perovskite/HTL interface has been minimized.

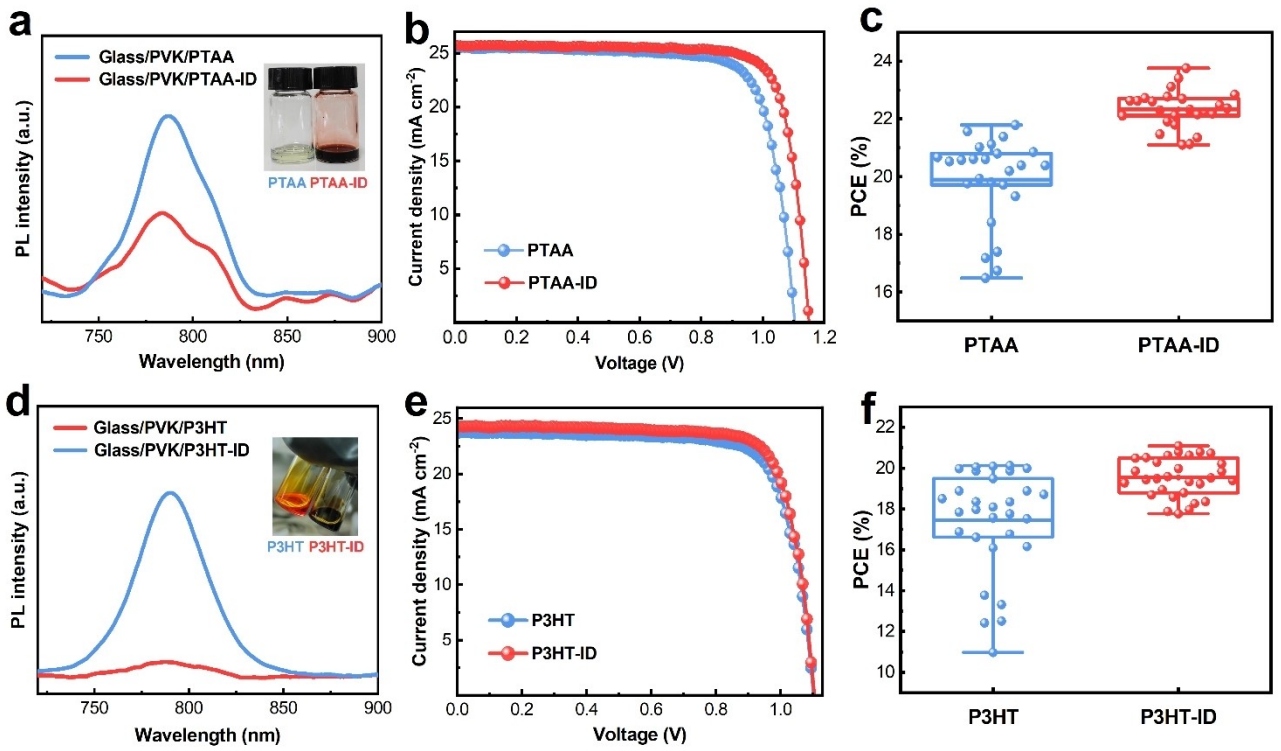

Figure 5. Performance of PSCs with π-conjugated polymers as HTL. (a) PL spectra of glass/perovskite/PTAA (PTAA-ID) films and the photo of PTAA (PTAA-ID) solution are shown in the inset. (b) Reverse *J–V* curves of champion PSCs with PTAA and PTAA-ID, the active area is 0.08 cm^2. (c) Statistical results of PCEs. (d) PL spectra of glass/perovskite/P3HT (P3HT-ID) films and the photo of P3HT (P3HT-ID) solution are shown in the inset. (e) Reverse *J–V* curves of champion PSCs with P3HT, and P3HT-ID, the active area is 0.08 cm^2. (f) Statistical results of PCEs.

Conclusions

In summary, we proposed a new doping strategy by constructing a cascade reaction in organic HTLs to achieve high-efficiency PSCs with high reproducibility. Owing to the dual functions of cascade reaction that is rapid and efficient oxidation and inhibition of perovskite sustained erosion from tBP, the PSCs with Spiro exhibit a champion PCE of 25.76 % (certificated of 25.38 %) with good reproducibility and stability. In addition, this doping strategy also shows excellent applicability in other organic HTLs, evidenced by the fact that the PTAA-based PSCs obtain a high PCE of 23.76 %. This work presents a subtle approach to overcome the tricky issue associated with the oxidation of organic HTL, which provides guidelines for achieving high-efficiency and high-reproducible PSCs and more opportunities to accelerate the commercialization of PSCs.

Supporting Information

Supporting Information is available from the Wiley Online Library or the author.

Acknowledgements

This work is supported partially by the Key Research and Development Program sponsored by the Ministry of Science and Technology (MOST) (Grant nos. 2022YFB4200301), National Natural Science Foundation of China (Grant nos. 52232008, 51972110, 52102245, and 52072121), Beijing Natural Science Foundation (2222076, 2222077), Beijing Science and Technology Planning Project (Z211100004621010), Beijing Nova Program (20220484016), Young Elite Scientists Sponsorship Program by CAST (2022QNRC001), 2022 Strategic Research Key Project of Science and Technology Commission of the Ministry of Education, Huaneng Group Headquarters Science and Technology Project (HNKJ20-H88), the Fundamental Research Funds for the Central Universities (2022MS029, 2022MS02, 2022MS031, 2023MS042) and the NCEPU "Double First-Class" Program.

Conflict of Interest

The authors declare no conflict of interest.

Data Availability Statement

The data that support the findings of this study are available from the corresponding author upon reasonable request.

Keywords: Perovskite · Solar cells · Hole transport layer · Oxidation · Reproducibility

[1] Best Research-Cell Efficiency Chart, *https://www.nrel.gov/pv/cell-efficiency.html*.
[2] F. Lin, J. Luo, Y. Zhang, J. Zhu, H. A. Malik, Z. Wan, C. Jia, *J. Mater. Chem. A* **2023**, *11*, 2544–2567.
[3] L. Yan, H. Huang, P. Cui, S. Du, Z. Lan, Y. Yang, S. Qu, X. Wang, Q. Zhang, B. Liu, X. Yue, X. Zhao, Y. Li, H. Li, J. Ji, M. Li, *Nat. Energy* **2023**, *8*, 1158–1167.
[4] S. Yu, Z. Xiong, H. Zhou, Q. Zhang, Z. Wang, F. Ma, Z. Qu, Y. Zhao, X. Chu, X. Zhang, J. You, *Science* **2023**, *382*, 1399–1404.
[5] J. P. Correa-Baena, A. Abate, M. Saliba, W. Tress, T. Jesper Jacobsson, M. Grätzel, A. Hagfeldt, *Energy Environ. Sci.* **2017**, *10*, 710–727.
[6] H. Huang, P. Cui, Y. Chen, L. Yan, X. Yue, S. Qu, X. Wang, S. Du, B. Liu, Q. Zhang, Z. Lan, Y. Yang, J. Ji, X. Zhao, Y. Li, X. Wang, X. Ding, M. Li, *Joule* **2022**, *6*, 2186–2202.
[7] P. Cui, D. Wei, J. Ji, H. Huang, E. Jia, S. Dou, T. Wang, W. Wang, M. Li, *Nat. Energy* **2019**, *4*, 150–159.
[8] U. B. Cappel, T. Daeneke, U. Bach, *Nano Lett.* **2012**, *12*, 4925–4931.
[9] J. Kong, Y. Shin, J. A. Röhr, H. Wang, J. Meng, Y. Wu, A. Katzenberg, G. Kim, D. Y. Kim, T. Li, E. Chau, F. Antonio, T. Siboonruang, S. Kwon, K. Lee, J. R. Kim, M. A. Modestino, H. Wang, A. D. Taylor, *Nature* **2021**, *594*, 51–56.
[10] J. Zhou, H. Li, L. Tan, Y. Liu, J. Yang, R. Hua, C. Yi, *Angew. Chem. Int. Ed.* **2023**, *62*, e202300314.
[11] T. Zhang, F. Wang, H. B. Kim, I. W. Choi, C. Wang, E. Cho, R. Konefal, Y. Puttisong, K. Terado, L. Kobera, M. Chen, M. Yang, S. Bai, B. Yang, J. Suo, S. C. Yang, X. Liu, F. Fu, H. Yoshida, W. M. Chen, J. Brus, V. Coropceanu, A. Hagfeldt, J. L. Brédas, M. Fahlman, D. S. Kim, Z. Hu, F. Gao, *Science* **2022**, *377*, 495–501.
[12] J. Y. Seo, S. Akin, M. Zalibera, M. A. R. Preciado, H. S. Kim, S. M. Zakeeruddin, J. V. Milić, M. Grätzel, *Adv. Funct. Mater.* **2021**, *31*, 2102124.
[13] S. Wang, M. Sina, P. Parikh, T. Uekert, B. Shahbazian, A. Devaraj, Y. S. Meng, *Nano Lett.* **2016**, *16*, 5594–5600.
[14] W. H. Nguyen, C. D. Bailie, E. L. Unger, M. D. McGehee, *J. Am. Chem. Soc.* **2014**, *136*, 10996–11001.
[15] X. Gao, F. Wu, Y. Zeng, K. Chen, X. Liu, L. Zhu, *J. Mater. Chem. C* **2023**, *11*, 11218–11224.
[16] Q. Liu, L. Fan, Q. E. Zhang, A. A. Zhou, B. Wang, H. Bai, Q. Tian, B. Fan, T. Zhang, *ChemSusChem* **2017**, *10*, 3098–3104.
[17] X. Wang, J. Wu, Y. Yang, G. Li, Z. Song, X. Liu, W. Sun, Z. Lan, P. Gao, *J. Energy Chem.* **2021**, *61*, 386–394.
[18] F. Ma, Y. Zhao, Z. Qu, S. Yu, Z. Chu, Z. Xiong, J. Zhou, Z. Wei, X. Zhang, J. You, *Solar RRL* **2023**, *7*, 2300042.
[19] H. Yang, T. Xu, W. Chen, Y. Wu, X. Guo, Y. Shen, C. Ding, X. Chen, H. Chen, J. Ding, X. Wu, G. Zeng, Z. Zhang, Y. Li, Y. Li, *Angew. Chem. Int. Ed.* **2024**, *63*, e202316183.
[20] F. Lamberti, T. Gatti, E. Cescon, R. Sorrentino, A. Rizzo, E. Menna, G. Meneghesso, M. Meneghetti, A. Petrozza, L. Franco, *Chem* **2019**, *5*, 1806–1817.
[21] W. Li, H. Dong, L. Wang, N. Li, X. Guo, J. Li, Y. Qiu, *J. Mater. Chem. A* **2014**, *2*, 13587–13592.
[22] Y. Han, G. Zhang, H. Xie, T. Kong, Y. Li, Y. Zhang, J. Song, D. Bi, *Nano Energy* **2022**, *96*, 107072.
[23] G. Ren, W. Han, Q. Zhang, Z. Li, Y. Deng, C. Liu, W. Guo, *Nano-Micro Lett.* **2022**, *14*, 175.
[24] A. Dasgupta, C. Thiehoff, P. D. Newman, T. Wirth, R. L. Melen, *Org. Biomol. Chem.* **2021**, *19*, 4852–4865.
[25] C. Ding, R. Huang, C. Ahläng, J. Lin, L. Zhang, D. Zhang, Q. Luo, F. Li, R. Österbacka, C. Ma, *J. Mater. Chem. A* **2021**, *9*, 7575–7585.
[26] X. Liu, B. Zheng, L. Shi, S. Zhou, J. Xu, Z. Liu, J. S. Yun, E. Choi, M. Zhang, Y. Lv, W. Zhang, J. Huang, C. Li, K. Sun, J. Seidel, M. He, J. Peng, X. Hao, M. Green, *Nat. Photonics* **2023**, *17*, 96–105.
[27] Q. Chen, J. Wu, X. Wang, G. Li, Z. Song, Y. Xu, C. Deng, Y. D. Weihai Sun, Z. Lan, *Chem. Eng. J.* **2022**, *450*, 138313.
[28] R. L. Forward, K. Y. Chen, D. M. Weekes, D. J. Dvorak, Y. Cao, C. P. Berlinguette, *ACS Energy Lett.* **2019**, *4*, 2547–2551.
[29] T. Wang, Y. Zhang, W. Kong, L. Qiao, B. Peng, Z. Shen, Q. Han, H. Chen, Z. Yuan, R. Zheng, X. Yang, *Science* **2022**, *377*, 1227–1232.
[30] D. Liu, C. Chen, X. Wang, X. Sun, B. Zhang, Q. Zhao, Z. Li, Z. Shao, X. Wang, G. Cui, S. Pang, *Adv. Mater.* **2023**, *n/a*, 2310962.
[31] P. Caprioglio, M. Stolterfoht, C. M. Wolff, T. Unold, B. Rech, S. Albrecht, D. Neher, *Adv. Energy Mater.* **2019**, *9*, 1901631.
[32] P. Metrangolo, L. Canil, A. Abate, G. Terraneo, G. Cavallo, *Angew. Chem. Int. Ed.* **2022**, *61*, e202114793.

Manuscript received: February 8, 2024
Accepted manuscript online: March 21, 2024
Version of record online: ■■, ■■

Research Articles

Solar Cells

Z. Lan, H. Huang, S. Du, Y. Lu, C. Sun, Y. Yang, Q. Zhang, Y. Suo, S. Qu, M. Wang, X. Wang, L. Yan, P. Cui, Z. Zhao,* M. Li* _____ e202402840

Cascade Reaction in Organic Hole Transport Layer Enables Efficient Perovskite Solar Cells

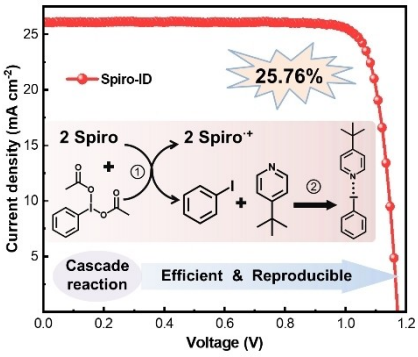

This work proposed a new doping strategy by constructing a cascade reaction in organic hole transport layer (HTL) to achieve high-efficiency perovskite solar cells (PSCs). Owing to the dual functions of cascade reaction that is rapid and efficient oxidation and inhibition of sustained erosion from 4-tert-butylpyridine to perovskite, the PSCs with Spiro-OMeTAD exhibit a champion power conversion efficiency of 25.76% (certificated of 25.38%) with good reproducibility and stability.